npj computational materials

www.nature.com/npjcompumats

ARTICLE OPEN

Check for updates

Machine learning molecular dynamics simulation identifying weakly negative effect of polyanion rotation on Li-ion migration

Zhenming Xu[1], Huiyu Duan[1], Zhi Dou[1], Mingbo Zheng[1]✉, Yixi Lin[1], Yinghui Xia[1], Haitao Zhao[2]✉ and Yongyao Xia[1,3]✉

Understanding the physical picture of Li ion transport in the current ionic conductors is quite essential to further develop lithium superionic conductors for solid-state batteries. The traditional practice of directly extrapolating room temperature ion diffusion properties from the high-temperature (>600 K) ab initio molecular dynamics simulations (AIMD) simulations by the Arrhenius assumption unavoidably cause some deviations. Fortunately, the ultralong-time molecular dynamics simulation based on the machine-learning interatomic potentials (MLMD) is a more suitable tool to probe into ion diffusion events at low temperatures and simultaneously keeps the accuracy at the density functional theory level. Herein, by the low-temperature MLMD simulations, the non-linear Arrhenius behavior of Li ion was found for Li_3ErCl_6, which is the main reason for the traditional AIMD simulation overestimating its ionic conductivity. The 1μs MLMD simulations capture polyanion rotation events in $Li_7P_3S_{11}$ at room temperature, in which four $[PS_4]^{3-}$ tetrahedra belonging to a part of the longer-chain $[P_2S_7]^{4-}$ group are noticed with remarkable rotational motions, while the isolated group $[PS_4]^{3-}$ does not rotate. However, no polyanion rotation is observed in $Li_{10}GeP_2S_{12}$, β-Li_3PS_4, Li_3ErCl_6, and Li_3YBr_6 at 300 K during 1μs simulation time. Additionally, the ultralong-time MLMD simulations demonstrate that not only there is no paddle-wheel effect in the crystalline $Li_7P_3S_{11}$ at room temperature, but also the rotational $[PS_4]^{3-}$ polyanion groups have weakly negative impacts on the overall Li ion diffusion. The ultralong-time MLMD simulations deepen our understanding of the relationship between the polyanion rotation and cation diffusion in ionic conductors at room environments.

npj Computational Materials (2023)9:105 ; https://doi.org/10.1038/s41524-023-01049-w

INTRODUCTION

Solid-state electrolyte (SSE) materials replacing the traditional flammable organic solvent electrolytes, can effectively combine with lithium metal anode and increase the safety and energy density of all-solid-state lithium ion batteries (ASSLIBs)[1,2]. For the practical application, lithium ionic conductivity at room temperature of an SSE material should be comparable to liquid electrolytes, more than 1mS cm^{-1}, and SSE materials are superionic conductors. Thus, deeply understanding the physical picture of ion transport in the current ionic conductors is the key to further optimizing and developing lithium superionic conductors as SSE materials. The current understandings of fast lithium diffusion in ionic conductors are mainly from two aspects: crystal structure[3,4] (static mechanics) and ion-lattice interaction dynamics[5,6]. Recently, some computational researches by the *ab*-initio molecular dynamics (AIMD) simulations show the coupled Li-ployanion dynamics between polyanion rotational motions and cation translational motions would enhance cation diffusion, called the paddle-wheel effect[7,8], including $0.75Li_2S$-$0.25P_2S_5$[9] glass, $Li_{3.25}P_{0.75}Si_{0.25}S_4$[10], $LiBF_4$[11] and $Na_{11}Sn_2PX_{12}$ (X = S and Se)[12] crystals. These AIMD simulations for lithium or sodium ionic conductors were mainly performed at elevated temperatures (>600 K) to enhance the sampling of ion diffusion events and obtain sufficient diffusion statistics at the time level of ~100 picoseconds (ps)[10,12], because the rare ion diffusion events in the low-temperature AIMD simulation would result in high statistical error. On the other hand, extrapolated room-temperature ionic conductivity and diffusivity by the Arrhenius assumption usually have large errors[13]. As these polyanion rotations and paddle-wheel effect are typically observed in the high-temperature phases with large free volumes and kinetic energies of atom, exploiting polyanion rotation in lithium ionic conductors at low temperatures is still a challenge. A question then naturally arises: whether polyanion rotation and even the paddle-wheel effect can persist down to the common ionic conductors at room temperature?

Today, the ab-initio calculation, molecular dynamics (MD) simulation and machine learning (ML) method are widely utilized for studying and developing advanced battery materials[14–16]. Especially for ML combine the classical computational methods, it is a powerful tool to efficiently predict properties and analyze the complex structure-function relationships of battery materials[17,18]. For example, Zhao et al. developed a ML prediction model enabling rational design and optimization of Li-argyrodites solid-state electrolytes based on the hierarchically encoding crystal structure-based descriptors[19,20], and Wang et al. combined the ab initio calculation and ML method to identify chemical factors affecting reaction kinetics in Li-O_2 battery, demonstrating the critical role of disorder degree of LiOH and solvent effect[21]. MD simulation based on the machine learning interatomic potential, so-called machine-learning molecular dynamics (MLMD) simulation, where energies and forces are directly obtained by solving the Schrödinger equation via the density functional theory (DFT) calculation, is a very powerful tool to extend the simulation time

[1]College of Materials Science and Technology, Nanjing University of Aeronautics and Astronautics, 210016 Nanjing, China. [2]Center for Intelligent and Biomimetic Systems, Shenzhen Institutes of Advanced Technology (SIAT), Chinese Academy of Sciences (CAS), 518055 Shenzhen, China. [3]Department of Chemistry and Shanghai Key Laboratory of Molecular Catalysis and Innovative Materials, Institute of New Energy, iChEm (Collaborative Innovation Center of Chemistry for Energy Materials), Fudan University, 200433 Shanghai, China. ✉email: zhengmingbo@nuaa.edu.cn; ht.zhao@siat.ac.cn; yongyaoxia@nuaa.edu.cn

scale from ps level to microsecond (μs) level and simultaneously keeps accuracy at the DFT level[22,23]. In this work, we first developed the machine-learning interatomic potentials for five lithium ionic conductors, including $Li_7P_3S_{11}$, $Li_{10}GeP_2S_{12}$, β-Li_3PS_4, Li_3ErCl_6 and Li_3YBr_6 (Fig. S1), and performed MLMD simulations at the time level of μs to capture polyanion rotation event and explore the paddle-wheel effect in above five lithium ionic conductors at 300 K, providing us a direct physical picture of the relationship between polyanion rotation and cation diffusion in ionic conductors at room temperature. Moreover, by MLMD simulations at low temperatures, we explored the non-Arrhenius behavior in these five lithium ionic conductors, which bridges the gap between experimental and simulated ionic conductivities.

RESULTS AND DISCUSSION

Performance of MTP potential

There are three major contradictions for reasonably and efficiently applying ML in material community, including contradictions between learning results and domain knowledge, between model complexity and ease of use, between high dimension and small sample data, which were firstly identified by Shi et al.[17,18,24]. Embedding domain knowledge of material science inside ML method to would effectively reconcile the above three contradictions. In this work, the domain knowledge of crystal structure, bond length and coordination environment of local atom is chosen as the structure descriptors to establish the mapping relationships between structure and energy (force). Fitting MTPs with respect to different lev_{max} values were considered, and the performance of MTPs predicted lattice constant, volume, and mean absolute errors (MAEs) in energies and forces are shown in Figs. S2–S11 in Supporting Information. Comprehensively considering the accuracy of predicted lattice constant and volume, MAEs in energies and forces are regarded to converge at lev_{max} of 10, 12, 10, 18, and 18, respectively for five lithium ionic conductors, as listed in Table 1, and MTPs for the following MLMD were based on these five lev_{max} values. In all cases, MAEs in energy are between 1.02 meV atom^{-1} and 3.86 meV atom^{-1}, while MAEs in force are less than 0.12 eV Å^{-1}. These MAEs are similar to or less than those of other MTPs fitted in the previous work[25,26], showing a remarkable improvement over the traditional interatomic potentials. Our MAEs in energy of the training and test data of $Li_7P_3S_{11}$ are larger than the previous work by S.P. Ong[27], but our MAEs in force are much close to them, 0.11 vs. 0.09. Additionally, viewed from Table 1, MAEs of the training and test data are generally very similar, demonstrating a little possibility of overfitting potentials. Our fitted MTPs would consistently exhibit high accuracy of reproducing DFT energies and forces at different temperatures. Table 2 compares lattice parameters and volumes for five lithium ionic conductors between MTP relaxations and experimental values. It can be seen that MTPs are generally able to reproduce lattice parameters and make absolute error less than 2.19% compared to experimental values, expect for $Li_7P_3S_{11}$. On the other hand, making comparison with the previous work of $Li_7P_3S_{11}$ by Ong[27], our MTP predicted lattice parameters and volume are much close to them. In all, our MTPs are reliable and well reproduce DFT energies and forces, lattice parameters, and local structures of these five lithium ionic conductors.

Table 1. Mean absolute errors (MAEs) of energy and force predictions for fitted MTPs of five lithium ionic conductors.

Materials	lev_{max}	MAEs in energy (eV atom^{-1})		MAEs in force (eV Å^{-1})	
		Training	Test	Training	Test
$Li_7P_3S_{11}$	10	3.86 (1.79)	3.81 (2.07)	0.12 (0.09)	0.11 (0.09)
$Li_{10}GeP_2S_{12}$	12	2.50	2.26	0.07	0.07
β-Li_3PS_4	18	2.00	2.00	0.07	0.07
Li_3ErCl_6	10	2.67	2.64	0.05	0.05
Li_3YBr_6	18	1.02	1.05	0.05	0.05

Values in brackets for $Li_7P_3S_{11}$ are listed for comparison, which are referred from the previous work predicted by MTPs[27].

Non-linear Arrhenius behavior

Based on the fitted MTPs, we performed low temperature MLMD simulations for five lithium ionic conductors. Figure 1 shows the Arrhenius plots and a summary of the derived activation energies (E_a) for Li ion diffusion. Viewed from the Arrhenius plots (filled markers and solid lines), four lithium ionic conductors, including $Li_7P_3S_{11}$, $Li_{10}GeP_2S_{12}$, β-Li_3PS_4 and Li_3YBr_6, exhibit the single linear Arrhenius behaviors from 300 K to 500 K, which is the traditional assumption made when extrapolating diffusivity from the high-temperature (>500 K) AIMD simulations to room temperature. While for Li_3ErCl_6, the non-linear Arrhenius behavior was observed, and the transition between the high-temperature (HT) quasi-linear regime with lower E_a (0.165 eV) and the low-temperature (LT) quasi-linear regime with higher E_a (0.425 eV) occurs at ~460 K. Therefore, following the traditional assumption of linear Arrhenius regime, directly extrapolating ionic conductivity at room temperature (σ_{300K}) from high-temperature (460–520 K) would cause a significant overestimation from 1.37 to 48.48 mS cm^{-1}. Our MLMD predicted E_a and σ_{300K} of 0.425 eV and 1.37 mS cm^{-1} for Li_3ErCl_6 is much close to the experiment determined results of 0.416 eV and 0.31 mS cm^{-1}[28], demonstrating that the near room temperature MLMD simulations well capture the transitions between quasi-Arrhenius regimes, and increase the accuracy of calculated σ_{300K}. To dig the reason behind the observed transitions between quasi-

Table 2. Lattice parameters and unit cell volumes of five lithium ionic conductors predicted by the trained MTPs at 0 K, in comparison with the experimental data at room temperature for $Li_7P_3S_{11}$[45], $Li_{10}GeP_2S_{12}$[64], β-Li_3PS_4[65], Li_3ErCl_6[28], and Li_3YBr_6[66].

Materials	*a* (Å)	*b* (Å)	*c* (Å)	Volume (Å^3)
$Li_7P_3S_{11}$	6.13 (1.72%)	12.63 (1.03%)	13.12 (4.70%)	837.33 (7.61%)
	6.19[27]	12.69[27]	12.86[27]	832.23[27]
$Li_{10}GeP_2S_{12}$	8.73 (0.15%)	8.73 (0.17%)	12.81 (1.62%)	976.06 (1.95%)
β-Li_3PS_4	6.20 (1.03%)	8.05 (0.01%)	13.22 (1.81%)	660.41 (2.85%)
Li_3ErCl_6	10.99 (1.59%)	10.99 (1.59%)	6.07 (0.56%)	634.94 (2.61%)
Li_3YBr_6	7.07 (2.19%)	11.94 (0.28%)	13.92 (1.42%)	1106.14 (3.34%)

Values in brackets are the percentage differences between the MTPs predicted values and the experimental measurements. For $Li_7P_3S_{11}$, the previous work predicted by MTPs are listed for comparison[27].

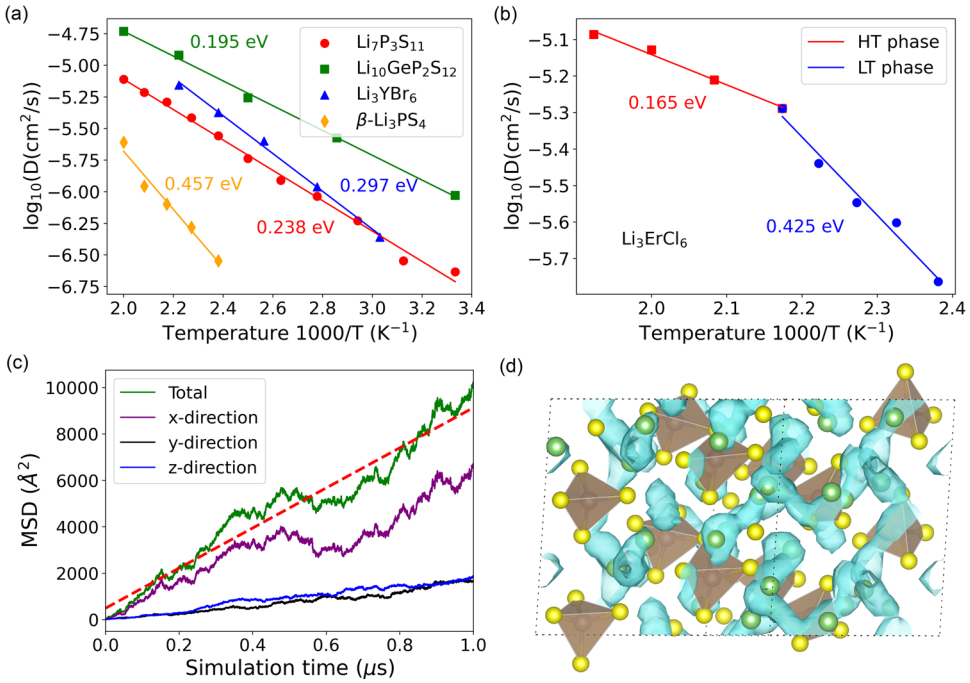

Fig. 1 Temperature-dependent Li ion diffusion coefficients by MLMD simulations of five lithium ionic conductors. a $Li_7P_3S_{11}$, $Li_{10}GeP_2S_{12}$, Li_3YBr_6 and β-Li_3PS_4 show the Arrhenius behaviors at low-temperature ranges of [300 K, 500 K], while **b** Li_3ErCl_6 exhibits the non-linear Arrhenius behavior at low-temperatures, and the transition occurs at 460 K. 1μs MLMD simulations for $Li_7P_3S_{11}$, **c** direction projected MSD curves of Li ion at 300 K, and **d** isosurfaces of the Li^+ probability density distribution P (light blue) at 300 K with $P = 0.0005$ a_0^{-3} (a_0 is the Bohr radius).

linear Arrhenius regimes of Li_3ErCl_6, Li trajectory lines from MLMD simulations near the transition temperature were extracted, as shown in Fig. S12. We noticed the order-disorder transition of Li ion sublattice. Below the transition temperature, Li ions primarily diffuse along *c*-axis direction, while additional Li ion diffusion paths along *a*-*b* planes are enabled above the transition temperature (500 K, Fig. S12b). These activated additional diffusion paths above 500 K increase the dimensionality for Li ion diffusion and decrease E_a from 0.425 eV to 0.165 eV.

Polyanion rotation

To capture sufficient Li diffusion and polyanion rotation events at room temperature, MLMD simulations for five lithium ionic conductors were performed at 300 K as long as 1μs. In $Li_7P_3S_{11}$, the maximum amplitude for Li vibration at room temperature is ~0.05 Å, and the mean amplitude is ~0.02 Å, as shown in Fig. S13. Figure 1c shows the total MSD and *x*-, *y*-, and *z*-direction projected MSD of Li ion diffusion in $Li_7P_3S_{11}$ as a function of simulation at 300 K. Total MSD of Li is about 10000 $Å^2$ after 1μs MLMD simulation, indicating considerable Li diffusion events in $Li_7P_3S_{11}$ at 300 K. The corresponding Li ion diffusion coefficient and ionic conductivity at room temperature are calculated to be 1.40×10^{-7} cm^2 s^{-1} and 14.96 mS cm^{-1}, respectively, much close to the experiment determined results of 1.65×10^{-7} cm^2 s^{-1} and 11.6–17 mS cm^{-1} [29,30] at 300 K. Due to the possible non-Arrhenius behavior, extrapolating room-temperature ion diffusivity and ionic conductivity by the Arrhenius assumption usually may cause large error. However, directly calculating Li ion diffusion coefficient and ionic conductivity from room temperature MLMD simulation would effectively reduce errors. Therefore, the calculated diffusion properties from room temperature MLMD simulation are more accurate and meaningful. We also note that the deviation between experiment value and our calculated Li ion diffusion coefficient of 2.3×10^{-7} cm^2 s^{-1} from 1 ns MLMD simulation is higher than that from 1μs MLMD simulation, demonstrating that extending simulation time to 1μs would significantly reduce the statistical errors of Li ion diffusion. Viewed from MSD data, Li ion diffusion along x-direction is more preferred than *y*- and *z*-directions, but it cannot illustrate $Li_7P_3S_{11}$ is a 1D ionic conductor at room temperature. In addition, isosurfaces of Li probability density distribution (Fig. 1d) clearly show 3D connected channels for Li ion diffusion. The good Li diffusivity provides sufficient diffusion events for us to explore the paddle-wheel effect in $Li_7P_3S_{11}$ at 300 K.

Compared to initial structure (Fig. 2a), significant polyanion rotations were noticed from last structure (Fig. 2b) of $Li_7P_3S_{11}$ after 1μs MLMD simulations at 300 K, including P5, P6, P7 and P8. For example, for central P8 atom, S4, S5 and S44 rotate about 120 or 240 degrees along P8-S28 bond axis (C_3 local symmetry axis), as depicted in Fig. 2c. During the whole MLMD simulation times, isolated $[PS_4]^{3-}$ group does not rotate, and all rotated $[PS_4]^{3-}$ tetrahedra belong to a part of the longer-chain $[P_2S_7]^{4-}$ group, in which one $[PS_4]^{3-}$ tetrahedron connects with its adjacent $[PS_4]^{3-}$ tetrahedron through a bridging S anion. This is different from the traditional understanding of the presence of longer-chain $[P_2S_7]^{4-}$ covalent network would impeding rotational behavior of $[PS_4]^{3-}$ tetrahedron and Li ion migration[9,31]. To further analyze the reason why $[PS_4]^{3-}$ tetrahedra from longer-chain $[P_2S_7]^{4-}$ group have better rotation abilities than simple $[PS_4]^{3-}$ group in $Li_7P_3S_{11}$, P-S bonding strengths were quantified by COHP and ICOHP analysis. Viewed from Fig. S14, -ICOHP value of P8-S28 bond is smaller than those of P8-S4 and P3-S11 bonds, demonstrating bonding strength of P-S pair with a bridging S anion is weaker than those P-S pairs with terminal S anions. On the other hand, bond lengths of 2.14–2.17 Å for P8-S28 are larger than 2.00–2.05 Å for other P-S bonds without bridge S atom. The longer bond length means the weaker bonding strength, in good accordance with the results of COHP calculations. These weak electronic interactions between P8 cation and S28 anion make P8-S28 bond effectively act as the rotation axis for $[PS_4]^{3-}$ tetrahedron.

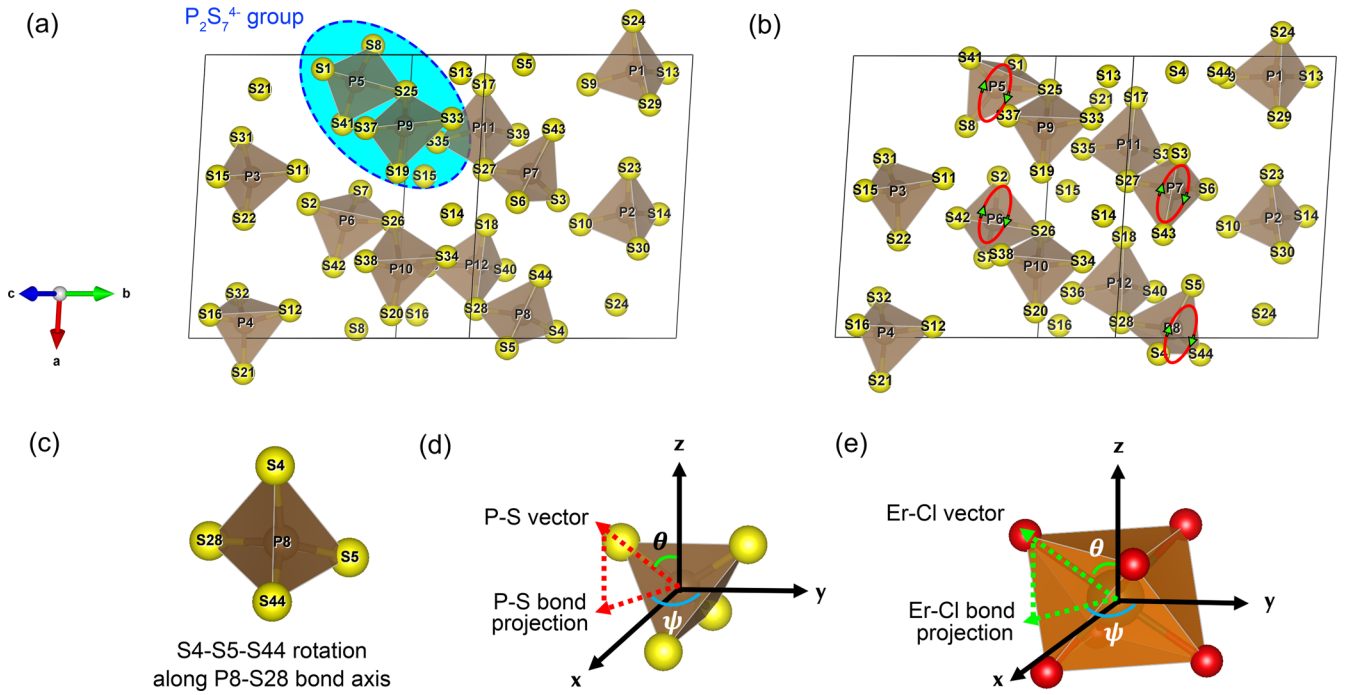

Fig. 2 1μs MLMD simulations for $Li_7P_3S_{11}$. a Initial crystal structure before MLMD simulations, **b** final structures with PS_4 polyanion rotations after 1μs MLMD simulations at 300 K, and **c** S4-S5-S44 in PS_4 polyanion rotating along P8-S28 bond axis. Schematic diagrams of the definition of angles θ and φ for **d** $[PS_4]^{3-}$ tetrahedron and **e** $[ErCl_6]^{3-}$ octahedron in the reference coordinate system. θ is defined as the angle between P–S or Er-Cl bond and *z*-axis, while angle φ corresponds to angle between the *y*-axis and the projection of P–S or Er-Cl bond vector in the *xy* plane.

Detailed analysis of atomic trajectories from 1μs MLMD simulations were performed to gain more comprehensive understanding of polyanion rotation in five lithium ionic conductors. To reduce computational expense for trajectory data analysis, here, crystal structure snapshots every 50 ps were extracted from 1μs MLMD simulations, and saved as atomic trajectory file. Figure S15 shows that P–S bond lengths in 5#, 6#, 7#, and 8# $[PS_4]^{3-}$ tetrahedron are fluctuating around 2.05 Å due to atomic vibrations or rotations during the whole 1 μs simulation time, and P-S bonds are well maintained even upon $[PS_4]^{3-}$ polyanion rotations, indicating that crystal structure is stable in dynamics at room temperature. To expediently monitor polyanion rotation during the whole MLMD simulation time, θ and φ angles were used as the indicators for $[PS_4]^{3-}$ and $[MX_6]^{3-}$ (M is transition metal, X is halogen) rotation, as depicted in Fig. 2d, e. Figure 3 shows the evolutions of θ and φ angles of four P-S bonds in 5#, 6#, 7# and 8# $[PS_4]^{3-}$ polyanions in $Li_7P_3S_{11}$ with respect to simulation time. It can be clearly seen that the remarkable exchanges in θ and φ angles occur at ~0.71 μs, ~0.71 μs, ~0.85 μs and ~0.92 μs for the first time, respectively for 5#, 6#, 7# and 8# $[PS_4]^{3-}$ polyanions. It reveals substantive rotations of $[PS_4]^{3-}$ polyanion in $Li_7P_3S_{11}$ at 300 K. Because of the room-temperature $[PS_4]^{3-}$ polyanion rotations usually occurring at the last two thirds of our 1 μs MLMD simulations, so it' is no wonder that the traditional room-temperature AIMD simulation at 300 ps level could not capture polyanion rotation in $Li_7P_3S_{11}$[32]. Figure 4 shows θ and φ angle evolutions of four P-S bonds in 7# and 8# $[PS_4]^{3-}$ tetrahedra from 918.05 ns to 918.20 ns with a time interval of 0.5 ps. It can be seen that a half rotation of three S ligands in $[PS_4]^{3-}$ polyanion over ~60 degrees occur within a very short time interval of ~3 ps, and a full rotation over 120 degrees for $[PS_4]^{3-}$ polyanion was finished in ~6 ps (from 918.137 ns to 918.143 ns), as Fig. S17 and video shown in Supporting Information. According to Li-Li average distance (Fig. S18) and Li diffusion coefficient (Fig. 1c), the estimated time scale of ~10 ns for a complete Li hopping between two stable Li sites at room temperature is much larger than a full $[PS_4]^{3-}$ rotation, indicating the correlation between $[PS_4]^{3-}$ rotation and Li ion translational motion is improbable at least on a time scale.

To quantitate the rotation dynamics, the Helmholtz free energies of four S anion ligands in $[PS_4]^{3-}$ polyanion (Fig. 5) were calculated from 2D probability distribution $\rho(\theta,\varphi)$ by mapping four S ligands in the spherical coordinates defined in Fig. 2d. The Helmholtz free energy surface reflects rotation routes by the coordinates of θ and φ, and rotational activation energy barriers by height difference between the local minima and transition states. It is worth noting that a remarkable $[PS_4]^{3-}$ rotation needs at least three S ligands simultaneously exchanging their spherical coordinates of θ and φ angles and staying at their adjacent minima, so at least three energy landscapes should be considered for each $[PS_4]^{3-}$ polyanion. It can be seen from Fig. 5 that for each $[PS_4]^{3-}$ polyanion, although one shallow energy landscape between two S ligands with a relatively low energy barrier (0.34 eV, 0.25 eV, 0.27 eV and 0.30 eV for 5#, 6#, 7# and 8# $[PS_4]^{3-}$ polyanion, respectively) is noticed, the overall energy barriers for 5#, 6#, 7#, and 8# $[PS_4]^{3-}$ polyanion rotational dynamics are in the range of 0.60–0.68 eV, which are much higher than those of Li diffusion in above lithium ionic conductors (Fig. 1), nonetheless close to Li diffusion in some common cathode materials, such as $LiCoO_2$ (0.73 eV)[33,34], $LiFePO_4$ (0.60 eV)[35,36], and $LiMn_2O_4$ (0.58 eV)[37]. In terms of such energy barrier magnitudes (0.60–0.68 eV), although the occurrence probability of $[PS_4]^{3-}$ polyanion rotations in $Li_7P_3S_{11}$ at room temperature is smaller than the translational motion of Li ion, rotating $[PS_4]^{3-}$ polyanion by the thermal activation stills relatively easy to produce, consistent with remarkable rotations in Figs. 3, 4, and S17 and video in Supporting Information.

Furthermore, the elevated temperature MLMD simulations of 350 K beyond room temperature were performed to explore enhanced $[PS_4]^{3-}$ polyanion rotations in $Li_7P_3S_{11}$, and the corresponding total simulation times are as the same as those

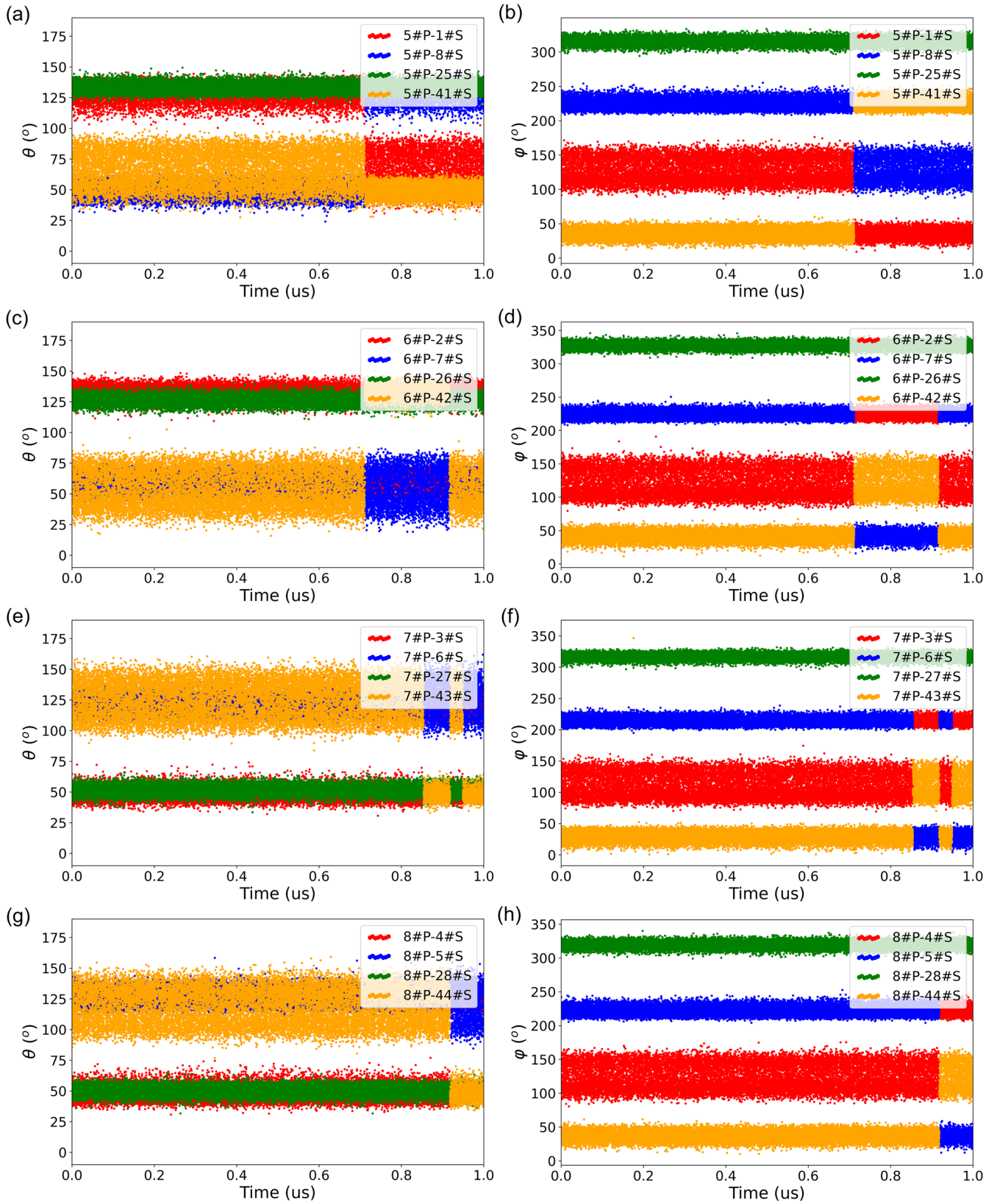

Fig. 3 Structural characteristic of PS_4 polyanion rotations during the whole 1μs MLMD simulations for $Li_7P_3S_{11}$ at 300 K. Angle θ and φ evolutions of the four P-S bonds in **a**, **b** 5#, **c**, **d** 6#, **e**, **f** 7#, and **g**, **h** 8# $[PS_4]^{3-}$ tetrahedra, respectively. Here, two adjacent data points with a time interval of 5 ps.

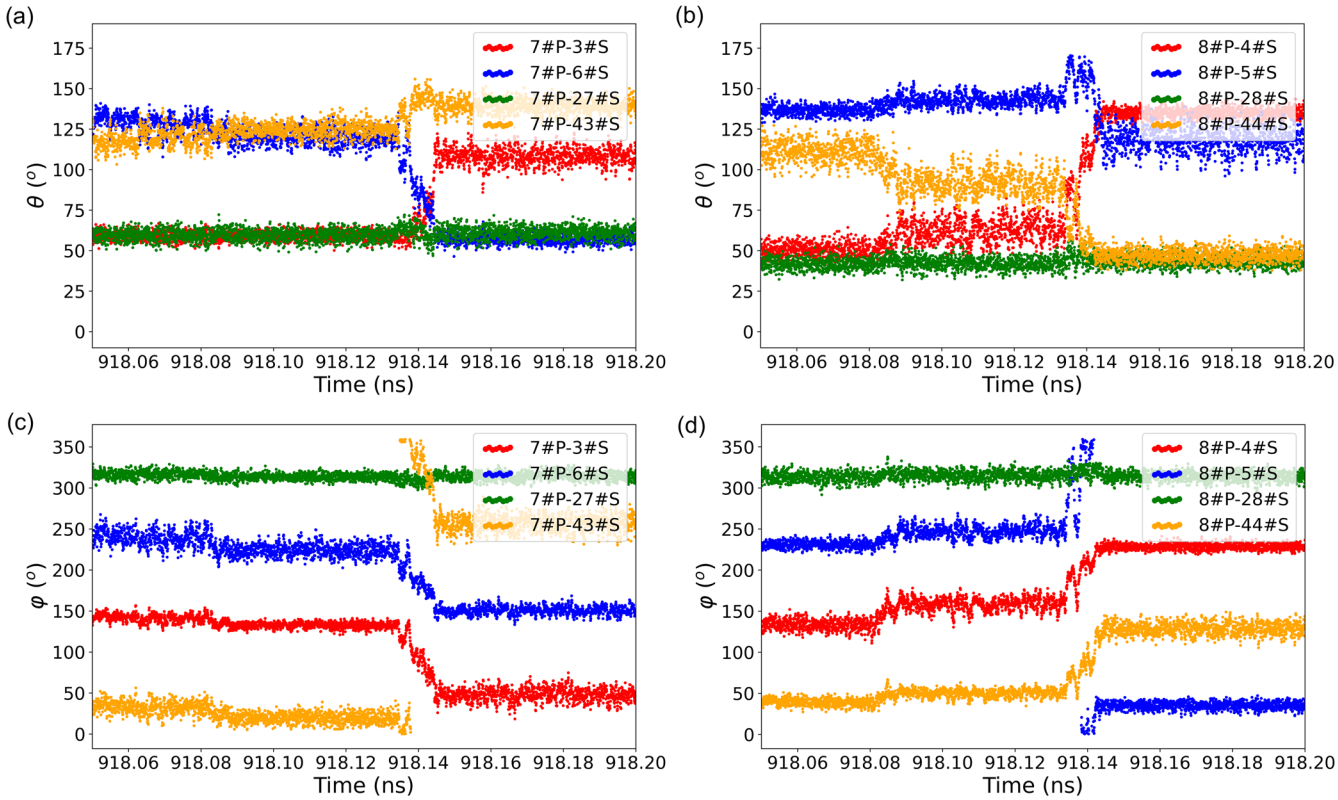

Fig. 4 Angle evolutions of P-S bonds. θ and φ evolutions of the four P-S bonds in **a**–**c** 7# and **b**–**d** 8# $[PS_4]^{3-}$ tetrahedra for $Li_7P_3S_{11}$ during 300 K MLMD simulations from 918.05 ns to 918.20 ns. Here, two adjacent data points with a time interval of 0.5 ps.

for 300 K. Figure S16 shows P-S bond lengths are fluctuating around 2.05 Å during the whole 1 μs simulation time, and all P-S bonds are well maintained even upon intense $[PS_4]^{3-}$ polyanion rotations, demonstrating stable structure dynamics at elevated temperature. Viewed from Fig. S20, for each 5#, 6#, 7#, and 8# $[PS_4]^{3-}$ tetrahedron, three S ligands continually exchange their spherical coordinates of θ and φ and stay at their adjacent minima during the whole 1 μs simulation time, indicating remarkable $[PS_4]^{3-}$ rotations in $Li_7P_3S_{11}$ at 350 K. Additionally, for each 5#, 6#, 7# and 8# $[PS_4]^{3-}$ tetrahedron, Helmholtz free energy surfaces (Fig. S21) clearly show flat energy landscapes among three S ligands, corresponding to the relatively low energy barriers (0.16–0.21 eV) for intensive $[PS_4]^{3-}$ rotations. Making a comparison between MLMD simulation results at 300 K and 350 K, $[PS_4]^{3-}$ rotational event in $Li_7P_3S_{11}$ is very sensitive to temperature change and thermal activation, and the occurrence frequency of rotation can be enhanced several times just by increasing 50 K. Therefore, extrapolating polyanion rotational events from elevated temperatures (>600 K) AIMD simulations to room temperature situation may cause some underlying deviations.

For other lithium conductors, 1μs MLMD simulations at 300 K were also performed, and the simulation results are shown in Figs. S22–S26. During the whole MLMD simulations time, no anion ligand exchanges its spherical coordinates of θ and φ, and no rotation at room temperature is observed for $[PS_4]^{3-}$ and $[GeS_4]^{4-}$ tetrahedron $Li_{10}GeP_2S_{12}$, $[PS_4]^{3-}$ tetrahedron in β-Li_3PS_4, $[ErCl_6]^{3-}$ octahedron in Li_3ErCl_6, and $[YBr_6]^{3-}$ octahedron in Li_3YBr_6, respectively. It should be noted that our MLMD simulations just demonstrate no remarkable polyanion rotation at room temperature during the 1μs simulation time, and polyanion rotations beyond 1μs cannot be completely ruled out for $Li_{10}GeP_2S_{12}$, β-Li_3PS_4, Li_3ErCl_6, and Li_3YBr_6 at 300 K. But certainly, the probability of occurrence of polyanion rotation in $Li_{10}GeP_2S_{12}$, β-Li_3PS_4, Li_3ErCl_6, and Li_3YBr_6 at room temperature is relatively much lower than $Li_7P_3S_{11}$.

The weakly negative effect of polyanion rotation on Li ion migration

To answer the question of whether $[PS_4]^{3-}$ polyanion rotation would effectively facilitate Li ion diffusion in $Li_7P_3S_{11}$ at 300 K, we further explored the relationships between $[PS_4]^{3-}$ polyanion rotation and Li ion translational motion. Figure 6a–d show 2D probability density distributions ($\rho^{2D}_{r,\theta}$) of P-S-Li angles θ and distance r between S ligands and their adjacent Li ions for rotational 5#-, 6#-, 7#- and 8#-$[PS_4]^{3-}$ polyanions. It is seen that $\rho^{2D}_{r,\theta}$ of four rotational $[PS_4]^{3-}$ polyanion systems are quite delocalized and dispersed in the most space of (r, θ), signifying the quite weak polyanion-cation dynamical couplings. On the other hand, if there is a strong polyanion-cation coupling dynamics, $\rho^{2D}_{r,\theta}$ would be localized in an agminated spot. Li ions in $Li_7P_3S_{11}$ are divided into two groups, that is Li ions in group-I are close to rotational $[PS_4]^{3-}$ polyanions, and Li ions in group-II are far away from rotational polyanions. Figure 6e shows e diffusion trajectories of Li ion in group-I near rotational 5#- and 6#-$[PS_4]^{3-}$ polyanions from 711.207 ns to 711.212 ns. During the rotation time of 5 ps, two $[PS_4]^{3-}$ polyanions successfully rotate 120 degrees, and Li ions in group-I close to these two polyanions also dramatically hop rather than vibration at their equilibrium sites, whose hopping distances are more than 1 Å. A similar phenomenon is observed for Li ion diffusion around rotational 7#- and 8#-$[PS_4]^{3-}$ polyanions from 918.137 ns to 918.143 ns, as depicted in Fig. 6g.

To quantitatively determine the correlations between $[PS_4]^{3-}$ polyanion rotation and Li ion translational diffusion, the Pearson correlation coefficients[38] between angular velocity vectors of S ligands in rotational 5#-, 6#-, 7#-, and 8#-$[PS_4]^{3-}$ polyanions and their adjacent Li ions were calculated, as shown in Fig. 6f, h. Here,

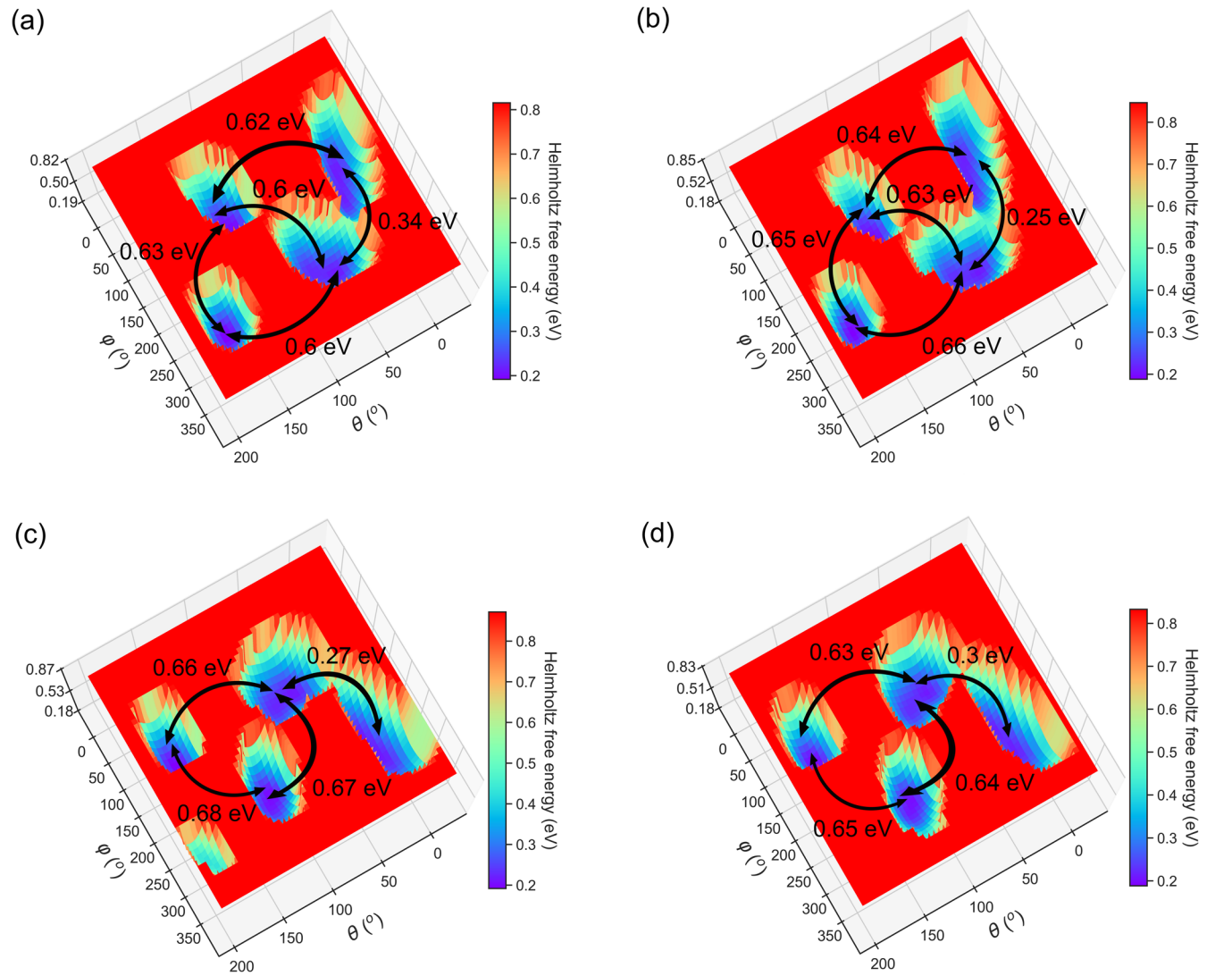

Fig. 5 Rotational dynamics of $[PS_4]^{3-}$ polyanion. The Helmholtz free energy surface of P-S bonds as a function of θ and φ angle for **a**, **b** 5#, **c**, **d** 6#, **e**, **f** 7#, and **g**, **h** 8# $[PS_4]^{3-}$ tetrahedron, respectively, from the whole 1μs MLMD simulations for $Li_7P_3S_{11}$ at 300 K. The free energy F was computed as $F(\theta,\varphi) = -k_B T \ln[\rho(\theta,\varphi)]$, where k_B is the Boltzmann constant, T is temperature, and $\rho(\theta, \varphi)$ is 2D projected probability distribution of four S ligands (as shown in Fig. S18 in Supporting Information).

only those Li ions staying within the first shell of $[PS_4]^{3-}$ during the whole rotation time are considered for the Pearson correlation coefficient calculations, whose P-Li distances are less than 4 Å, referred from RDF of P-Li in Fig. S18. All the absolute values of calculated Pearson correlation coefficient are less than 0.25. Given that a Pearson correlation coefficient smaller than 0.5 is generally regarded as weak in statistics[39], so Li ion translational diffusion is quite weakly correlated to rotational $[PS_4]^{3-}$ polyanions. Furthermore, diffusion coefficients of Li group-I near and Li group-II far away from rotational polyanions were determined to get detailed diffusion events, as shown in Fig. 6i–l. It is found that diffusion coefficients of Li group-II far away from $[P_2S_7]^{4-}$ are smaller than those of Li group-I near $[P_2S_7]^{4-}$. As Fig. S27 shows that the calculated anion charges of S ligands in $[P_2S_7]^{4-}$ are smaller than those of isolated $[PS_4]^{3-}$ groups, especially for the bridging S anion with a charge of −0.57 *e*, so the electrostatic attractions between $[P_2S_7]^{4-}$ polyanion group and Li^+ cation are relatively weaker[40–42], eventually leading to higher diffusion diffusivities.

On the other hand, most importantly, diffusion coefficients of both Li groups near and far away from rotational 5#-, 6#-, 7#-, and 8#-$[PS_4]^{3-}$ polyanions unanimously exhibit downtrends within $[PS_4]^{3-}$ rotation time. Because the Li-anion electrostatic interactions are long-ranged, rotational $[PS_4]^{3-}$ polyanions also have impacts on those Li ions far away from them. In other words, the rotation of $[PS_4]^{3-}$ polyanion groups would lower the instantaneous Li ion diffusivities of all ions in unit cell, which may be due to the contingent inconsistency of direction between Li ion translational motion and polyanion rotation disturbing the potential energy surface of Li with respect to $[PS_4]^{3-}$ polyanion rotation. It is fully consistent with our previous results of anharmonic phonon calculations for crystalline $Li_7P_3S_{11}$[43], that is the low-frequency $[PS_4]^{3-}$ rotational modes anharmonically couple with high-frequency Li modes, which vibrate toward S-S edge or along Li-S apex and are not Li diffusion pathways. The phenomenon of decoupled $[PS_4]^{3-}$ rotational motion from Li jump is also observed in $70Li_2S$-$30P_2S_5$ glass system[32]. Therefore, from our MLMD simulations at 300 K, it can be concluded here that there is no paddle-wheel effect in the crystalline $Li_7P_3S_{11}$ at room temperature, and rotational $[PS_4]^{3-}$ polyanion groups at 5–6 ps level have some weakly negative impacts on the overall Li ion diffusion in $Li_7P_3S_{11}$ unit cell. In fact, lack of paddle-wheel effect is also reported for BH_4-substituted Li argyrodite system[44]. Compare

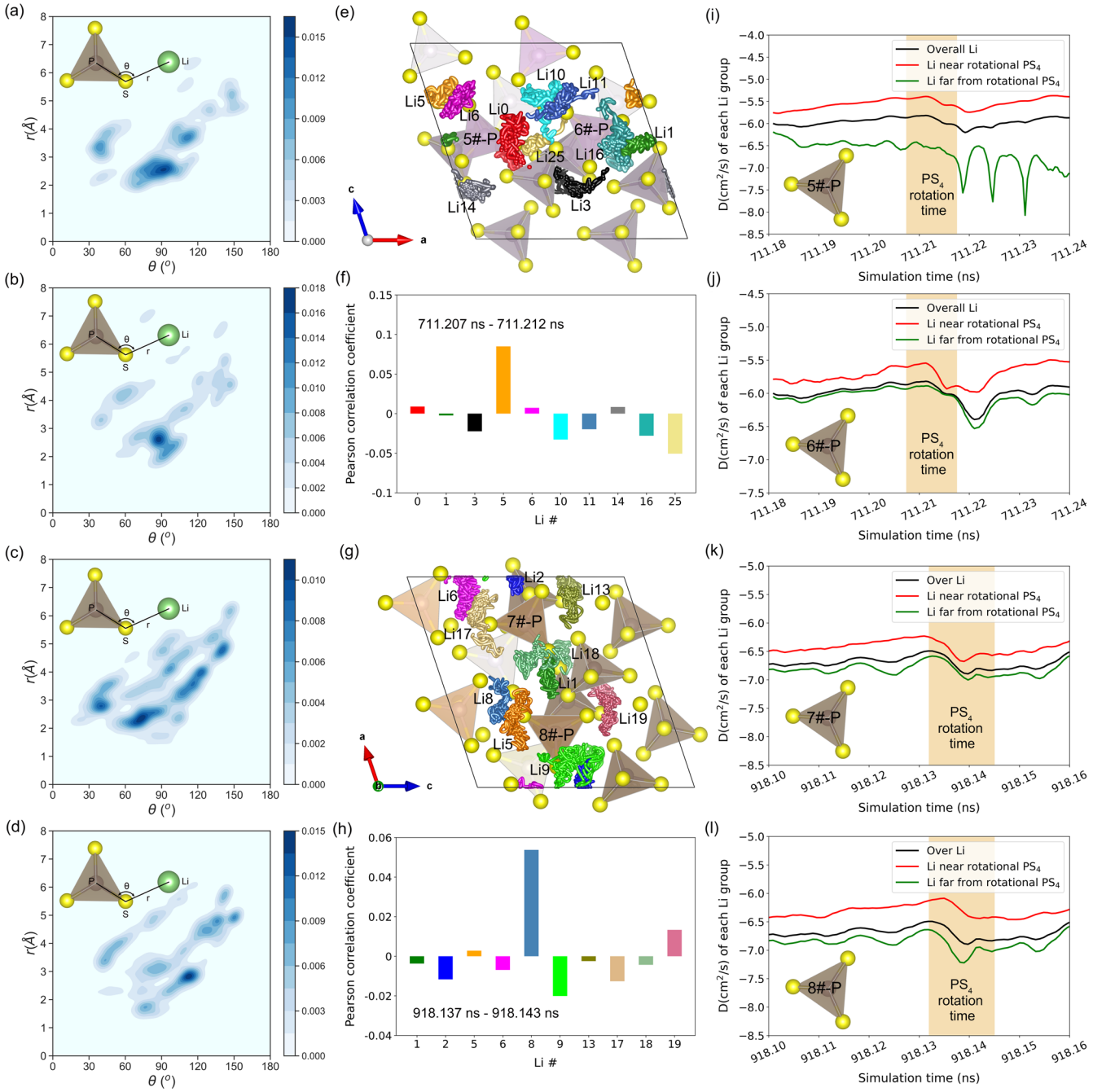

Fig. 6 The relationships between $[PS_4]^{3-}$ polyanion groups (5#-P, 6#-P, 7#-P and 8#-P) and their adjacent Li ions during $[PS_4]^{3-}$ rotation time for 300 K MLMD simulations of $Li_7P_3S_{11}$. 2D probability density distribution ($\rho^{2D}_{r,\theta}$) of P-S-Li angles θ and distance r between S ligands and Li ion in the first shell of **a** 5#-, **b** 6#-, **c** 7#-, and **d** 8#-$[PS_4]^{3-}$ polyanions, respectively; **e** diffusion trajectories of each Li ion near rotational 5#- and 6#-$[PS_4]^{3-}$ polyanions; **f** Pearson correlation coefficients between angular velocity vectors of S ligands in rotational 5#- and 6#-$[PS_4]^{3-}$ polyanions and their adjacent Li ions; **g** diffusion trajectories of each Li ion near rotational 7#- and 8#-$[PS_4]^{3-}$ polyanions; **h** Pearson correlation coefficients between angular velocity vectors of S ligands in rotational 7#- and 8#-$[PS_4]^{3-}$ polyanions and their adjacent Li ions; evolutions of diffusion coefficient for Li groups near and far away from rotational **i** 5#-, **j** 6#-, **k** 7#-, and **l** 8#-$[PS_4]^{3-}$ polyanions, respectively.

to other sulfides (Table S1), the superionic conductivity of for $Li_7P_3S_{11}$ mainly owes to its highly distorted LiS_n polyhedron and the weak Li-anion Coulomb force providing the frustrated potential energy surface for Li ion migration with low activation energy barrier[4]. Li ion migration in $Li_7P_3S_{11}$ benefit from bridging S anions from longer-chain $[P_2S_7]^{4-}$ units rather than rotations of $[PS_4]^{3-}$ polyanion from them.

In this work, the machine-learning interatomic potentials based on the MTP framework were developed for $Li_7P_3S_{11}$, $Li_{10}GeP_2S_{12}$, β-Li_3PS_4, Li_3ErCl_6, and Li_3YBr_6 lithium ionic conductors. The newly developed machine-learning interatomic potentials well reproduce the DFT energies and forces, lattice parameters, and local structures of these five lithium ionic conductors. Combining the classical molecular dynamics simulations with our developed machine-learning interatomic potentials, the ultralong-time MLMD simulations were performed for five lithium ionic conductors at near room temperature and other elevated temperatures, which enhance the sampling of Li diffusion events and reduce

calculation errors. On one hand, MLMD simulations show $Li_7P_3S_{11}$, $Li_{10}GeP_2S_{12}$, β-Li_3PS_4, and Li_3YBr_6 exhibit the linear Arrhenius behaviors from 300 K to 500 K. While for Li_3ErCl_6, the non-linear Arrhenius behavior was observed, and the corresponding phase transition occurs at ~460 K. The near room temperature MLMD simulations well capture the non-linear Arrhenius behavior and would increase the accuracy of calculated ionic conductivity at room temperature. On the other hand, the simulation time of 300 K MLMD simulations was extended to 1 μs level to capture sufficient Li diffusion and polyanion rotation events in lithium ionic conductors at room temperature. MLMD simulation results demonstrate no remarkable polyanion rotation in $Li_{10}GeP_2S_{12}$, β-Li_3PS_4, Li_3ErCl_6, and Li_3YBr_6 at room temperature during 1μs simulation time, just librational motion for them. However, in $Li_7P_3S_{11}$ at room temperature, four $[PS_4]^{3-}$ tetrahedron in unit cell are noticed with remarkable rotational motions. All the rotated $[PS_4]^{3-}$ tetrahedra belong to a part of the longer-chain $[P_2S_7]^{4-}$ group, while isolated group $[PS_4]^{3-}$ does not rotate. Moreover, a full rotation of three S ligands in $[PS_4]^{3-}$ polyanion over ~120 degrees was finished in 5–6 ps. Lastly, our 300 K MLMD simulations show Li ion translational diffusion is quite weakly correlated to the rotation of $[PS_4]^{3-}$ polyanions in $Li_7P_3S_{11}$, and rotational $[PS_4]^{3-}$ polyanion groups at 5–6 ps level have some weakly negative impacts on the overall Li ion diffusion. There is no paddle-wheel effect in the crystalline $Li_7P_3S_{11}$ at room temperature, and Li ion migration in $Li_7P_3S_{11}$ benefits from bridging S anions from longer-chain $[P_2S_7]^{4-}$ units rather than rotations of $[PS_4]^{3-}$ polyanion from them. In short, our ultralong-time MLMD simulations at low temperatures effectively capture the polyanion rotation events and identify no paddle-wheel effect in $Li_7P_3S_{11}$ at room temperature, deepening our understanding of the relationship between polyanion rotation and cation diffusion in ionic conductors at room environment.

METHODS

Crystal structures

Supercells of $Li_7P_3S_{11}$, $Li_{10}GeP_2S_{12}$, β-Li_3PS_4, Li_3ErCl_6 and Li_3YBr_6 with lattice parameters greater than 10 Å were constructed to minimize interactions between two periodic images. For $Li_7P_3S_{11}$, a 1 × 2 × 1 supercell with 84 atoms was constructed from the experimentally determined crystal structure by Yamane et al.[45]. For $Li_{10}GeP_2S_{12}$, a 2 × 2 × 1 supercell with 200 atoms was created from the computed structure in Materials Project (MP) database (mp-696138). For Li_3ErCl_6 and Li_3YBr_6, starting from the experimentally reported disordered structures with fractional occupancies, the 1 × 1 × 2 and 2 × 1 × 1 supercells with 60 and 80 atoms were firstly built, respectively, and then all Li-vacancy cation configurations were created using the enumeration method[46] implemented in Pymatgen code[47]. Lastly, the most stable Li-vacancy configuration of Li_3ErCl_6 and Li_3YBr_6 were determined by ranking their DFT energies, and the corresponding space groups are P321 and C2/c, respectively.

DFT calculations and AIMD simulations

All calculations were carried out in the framework of density functional theory (DFT)[48] using the projector augmented wave method[49], as implemented in Vienna ab-initio Simulation Package (VASP). The generalized gradient approximation (GGA)[50] and Perdew–Burke–Ernzerhof (PBE) exchange functional were employed. The plane-wave energy cutoff was set to 520 eV, and a k-point density of at least 64/$Å^{-3}$, similar to those used in the MP database. AIMD calculations were performed without spin-polarization in an NPT ensemble at elevated temperatures with a Nose−Hoover thermostat[51]. A smaller plane wave energy cut-off of 300 eV was chosen for AIMD simulations of the supercells with a Gamma-centered 1 × 1 × 1 k-point grid, and the simulation supercell sizes were at least 10 Å along each lattice direction. Time step was set to 2 fs, and all supercell systems were simulated for a short time with a total of 10,000 steps. AIMD simulations with supercell model were performed at six different temperatures (from 300 to 1300 K with 200 K intervals) to diversify the training structures. For each temperature, about 300 snapshot structures were uniformly extracted from the production run of 20 ps. Hence, for each lithium ionic conductor, a total of 1800 training structures (300 × 6 temperatures) were generated. To obtain accurate energies and forces for machine learning potential training, the static self-consistent field (SCF) calculations for training structures were carried out. These SCF calculations were performed with a higher k-point density of at least 100/$Å^{-3}$, an energy cutoff of 520 eV. The convergence criterion of energy for SCF calculations was set to 10^{-6} eV $atom^{-1}$. The crystal orbital Hamilton population (COHP) between neighboring oxygen ions was computed by Lobster program[52], in which the negative and positive COHP values indicate bonding and anti-bonding, respectively. Integrating COHP to Fermi energy level obtain -ICOHP data to quantify the chemical bonding strength. The pbeVaspFit2015 basis sets were used for the reconstruction of the PAW wave functions of each element.

MTP model training and verification

Today, there are many machine-learning atomic potential models, such as the neural network potential (NNP)[53], the Gaussian approximation potential (GAP)[54], the moment tensor potentials (MTP)[55], the smooth overlap of atomic positions (SOAP)[56] and the spectral neighbor analysis potential (SNAP)[57]. According to the previous work by S.P. Ong et al.[25], MTP model exhibits the smallest root-mean-square errors in energies and forces. MD simulations based on the MTP framework have been successfully applied to many battery materials, including metals[58], cathode coating materials[26] and SSE materials[27]. We sure that MTP model is the best model for our work, when considering a trade-off between accuracy and computational cost. In this work, the energy and force data points are assigned weights of 100:1, similar to the previous work by Ong[27]. In the MTP framework, two key parameters should be carefully selected, which determine the potential performance, including radius cutoff (R_{cut}) and maximum level (lev_{max}). The radius cutoff R_{cut} controls the maximum interaction range between atoms, in this work, R_{cut} for our five lithium ionic conductors are set to 5 Å, a typical value used in previously reported MTP frameworks[26,27,58]. The maximum level (lev_{max}) determines completeness of the basis set functions, the larger lev_{max} would make the larger number of terms in the linear expansion, in turn resulting in higher computational loading and a greater possibility of over-fitting. In this work, lev_{max} for our five lithium ionic conductors were tested among these five values of 8, 10, 12, 14, 16 and 18. For the potential fitting, an 80:20 split of the training : test data was used. All training, evaluations and simulations with MTP framework were performed by using the open-source software and Python packages, including MLIP[59], LAMMPS[60] and Materials Machine Learning (maml).

Diffusivity and activation barrier calculations

Classical MD simulations for five lithium ionic conductors were performed by LAMMPS interfaced with the trained MTPs, called machine learning driven molecular dynamics (MLMD). The supercells of five lithium ionic conductors for MLMD simulations are the same as those of AIMD simulations. Time step was set to 1 fs, a typical value used in the previous work[61]. Each lithium ionic conductor was firstly equilibrated in the NPT ensemble for 100 ps, and then equilibrated in the NVT ensemble for 1 million steps (total simulation time as long as 1 ns). Lattice volumes for MLMD simulations in the NVT ensemble were averaged from all structures of the previous MLMD simulations in the NPT ensemble.

For each material, MLMD simulations were performed at room and slightly elevated temperatures (from 300 to 520 K). At each temperature, MLMD simulations were repeated 20 times to enhance samplings of diffusion events and reduce the calculation errors.

Diffusional properties of an atom can be calculated from its MLMD trajectories with positions of r_i(t), and the displacement Δr_i of *i*-th particle from time t_1 to t_2 can be calculated by $\Delta r_i(\Delta t) = r_i(t_2) - r_i(t_1)$, where $\Delta t = t_2 - t_1$. Total squared displacements are obtained by summing the squared displacements of all *N* mobile atoms over a time interval Δt, $\sum_{i=1}^{N}(|\Delta r_i(\Delta t)|^2)$. Over a total MLMD simulation time duration of t_{total}, there are many time intervals of $N_{\Delta t}$ with the same duration of Δt ($\Delta t < t_{\text{total}}$) at different starting time of *t*. Due to atom's displacements over Δt reflecting mobility of atoms, the total mean squared displacements (TMSDs) of all *N* mobile atoms over a time interval of Δt can be obtained by calculating the statistical ensemble average of the squared displacements over a total of $N_{\Delta t}$ time intervals with the same duration of Δt[62], $\text{TMSD}(\Delta t) = \sum_{i=1}^{N}\langle|r_i(\Delta t) - r_i(0)|^2\rangle = \sum_{N}^{N}\frac{1}{N_{\Delta t}}\sum_{t=0}^{t_{total}-\Delta t}|r_i(t+\Delta t) - r_i(t)|^2$, where $\langle\cdot\rangle$ stands for the statistical ensemble average. This statistical ensemble average over different time intervals of $N_{\Delta t}$ offers the statistical analysis of sufficient diffusional events to obtain accurate diffusional properties. To get diffusivity of the mobile species, MSD over time interval of Δt is calculated by averaging TMSDs to each mobile atom, $\text{MSD}(\Delta t) = \text{TMSDs}(\Delta t)/N$, where, *N* is the number of mobile atoms.

If MLMD simulations contain the sufficient diffusional events, the dependence of MSD over time intervals of Δt would follow a linear relationship. According to the Einstein relation, self-diffusion coefficient *D* of a specie can be calculated from the slope of MSD curve as a function of time intervals Δt [63], $D = \frac{\text{MSD}(\Delta t)}{2d\Delta t}$, where, $d = 3$ is the diffusion dimension of a particle in simulated system. The linear fitting of MSD vs. Δt to the Einstein relation should only be performed on the linear region corresponding to good diffusional displacements. Therefore, to achieve small error bounds of the fitted *D* and get accurate diffusivity, MLMD simulations should be long enough for capturing a large number of diffusion events. Performing a series of MLMD simulations at different temperatures obtains the Arrhenius relations of the log of diffusivity *D* as a function of 1/*T*, $D = D_0(-E_a/k_BT)$, and which can extrapolate the prefactor D_0, overall activation energy E_a, diffusivity *D* and conductivity σ at RT.

DATA AVAILABILITY

Data supporting the work are available from the corresponding author on reasonable request.

CODE AVAILABILITY

Codes are available from the corresponding author on reasonable request.

Received: 6 January 2023; Accepted: 15 May 2023;
Published online: 17 June 2023

REFERENCES

1. Ye, T., Li, L. & Zhang, Y. Recent progress in solid electrolytes for energy storage devices. *Adv. Funct. Mater.* **30**, 2000077 (2020).
2. Kim, K. J., Balaish, M., Wadaguchi, M., Kong, L. & Rupp, J. L. M. Solid-state Li–metal batteries: challenges and horizons of oxide and sulfide solid electrolytes and their interfaces. *Adv. Energy Mater.* **11**, 2002689 (2020).
3. Wang, Y. et al. Design principles for solid-state lithium superionic conductors. *Nat. Mater.* **14**, 1026 (2015).
4. Di Stefano, D. et al. Superionic diffusion through frustrated energy landscape. *Chem* **5**, 1–11 (2019).
5. Muy, S. et al. Tuning mobility and stability of lithium ion conductors based on lattice dynamics. *Energy Environ. Sci.* **11**, 850–859 (2018).
6. Sagotra, A. K., Chu, D. & Cazorla, C. Influence of lattice dynamics on lithium-ion conductivity: a first-principles study. *Phys. Rev. Mater.* **3**, 035405 (2019).
7. Jansen, M. Volume effect or paddle-wheel mechanism—fast alkali-metal ionic conduction in solids with rotationally disordered complex anions. *Angew. Chem. Int. Ed. Engl.* **30**, 1547–1558 (1991).
8. Zhang, Z. & Nazar, L. F. Exploiting the paddle-wheel mechanism for the design of fast ion conductors. *Nat. Rev. Mater.* **7**, 389–405 (2022).
9. Smith, J. G. & Siegel, D. J. Low-temperature paddlewheel effect in glassy solid electrolytes. *Nat. Commun.* **11**, 1483 (2020).
10. Zhang, Z. et al. Targeting superionic conductivity by turning on anion rotation at room temperature in fast ion conductors. *Matter* **2**, 1667–1684 (2020).
11. Wu, S., Xiao, R., Li, H. & Chen, L. New insights into the mechanism of cation migration induced by cation–anion dynamic coupling in superionic conductors. *J. Mater. Chem. A* **10**, 3093–3101 (2022).
12. Zhang, Z., Roy, P. N., Li, H., Avdeev, M. & Nazar, L. F. Coupled cation-anion dynamics enhances cation mobility in room-temperature superionic solid-state electrolytes. *J. Am. Chem. Soc.* **141**, 19360–19372 (2019).
13. He, X., Zhu, Y., Epstein, A. & Mo, Y. Statistical variances of diffusional properties from ab initio molecular dynamics simulations. *npj Comput. Mater.* **4**, 1–9 (2018).
14. Shi, S. et al. Multi-scale computation methods: their applications in lithium-ion battery research and development. *Chin. Phys. B* **25**, 018212 (2016).
15. Urban, A., Seo, D.-H. & Ceder, G. Computational understanding of Li-ion batteries. *npj Comput. Mater.* **2**, 16002 (2016).
16. Liu, B. et al. Rationalizing the interphase stability of Li|doped-Li7La3Zr2O12via automated reaction screening and machine learning. *J. Mater. Chem. A* **7**, 19961–19969 (2019).
17. Liu, Y., Wu, J. M., Avdeev, M. & Shi, S. Q. Multi-layer feature selection incorporating weighted score-based expert knowledge toward modeling materials with targeted properties. *Adv. Theory Simul.* **3**, 1900215 (2020).
18. Liu, Y., Zhao, T., Ju, W. & Shi, S. Materials discovery and design using machine learning. *J. Materiomics* **3**, 159–177 (2017).
19. Zhao, Q. et al. Identifying descriptors for Li+ conduction in cubic Li-argyrodites via hierarchically encoding crystal structure and inferring causality. *Energy Storage Mater.* **40**, 386–393 (2021).
20. Zhao, Q., Avdeev, M., Chen, L. & Shi, S. Machine learning prediction of activation energy in cubic Li-argyrodites with hierarchically encoding crystal structure-based (HECS) descriptors. *Sci. Bull.* **66**, 1401–1408 (2021).
21. Wang, A. et al. Identifying chemical factors affecting reaction kinetics in Li-air battery via ab initio calculations and machine learning. *Energy Storage Mater.* **35**, 595–601 (2021).
22. Xu, Z. & Xia, Y. Progress, challenges and perspectives of computational studies on glassy superionic conductors for solid-state batteries. *J. Mater. Chem. A* **10**, 11854–11880 (2022).
23. Unke, O. T. et al. Machine learning force fields. *Chem. Rev.* **121**, 10142–10186 (2021).
24. Liu, Y., Guo, B., Zou, X., Li, Y. & Shi, S. Machine learning assisted materials design and discovery for rechargeable batteries. *Energy Storage Mater.* **31**, 434–450 (2020).
25. Zuo, Y. et al. Performance and cost assessment of machine learning interatomic potentials. *J. Phys. Chem. A* **124**, 731–745 (2020).
26. Wang, C., Aoyagi, K., Wisesa, P. & Mueller, T. Lithium ion conduction in cathode coating materials from on-the-fly machine learning. *Chem. Mater.* **32**, 3741–3752 (2020).
27. Qi, J. et al. Bridging the gap between simulated and experimental ionic conductivities in lithium superionic conductors. *Mater. Today Phys.* **21**, 100463 (2021).
28. Schlem, R. et al. Mechanochemical synthesis: a tool to tune cation site disorder and ionic transport properties of Li_3MCl_6 (M = Y, Er) superionic conductors. *Adv. Energy Mater.* **10**, 1903719 (2019).
29. Chu, I. H. et al. Insights into the performance limits of the $Li_7P_3S_{11}$ superionic conductor: a combined first-principles and experimental study. *ACS Appl. Mater. interfaces* **8**, 7843–7853 (2016).
30. Seino, Y., Ota, T., Takada, K., Hayashi, A. & Tatsumisago, M. A sulphide lithium super ion conductor is superior to liquid ion conductors for use in rechargeable batteries. *Energy Environ. Sci.* **7**, 627–631 (2014).
31. Dietrich, C. et al. Lithium ion conductivity in Li_2S–P_2S_5 glasses – building units and local structure evolution during the crystallization of superionic conductors Li_3PS_4, $Li_7P_3S_{11}$ and $Li_4P_2S_7$. *J. Mater. Chem. A* **5**, 18111–18119 (2017).
32. Ohkubo, T., Ohara, K. & Tsuchida, E. Conduction mechanism in $70Li_2S$-$30P_2S_5$ glass by ab initio molecular dynamics simulations: comparison with $Li_7P_3S_{11}$ crystal. *ACS Appl. Mater. interfaces* **12**, 25736–25747 (2020).
33. Lee, H.-S. et al. Atomic structure and defect energetics of LiCoO2 grain boundary. *Mater. Res. Bull.* **82**, 81–86 (2016).
34. Moriwake, H. et al. First-principles calculations of lithium-ion migration at a coherent grain boundary in a cathode material, LiCoO2. *Adv. Mater.* **25**, 618–622 (2013).

35. Ouyang, C., Shi, S., Wang, Z., Huang, X. & Chen, L. First-principles study of Li ion diffusion in LiFePO4. *Phys. Rev. B* **69**, 104303 (2004).
36. Zaghib, K., Mauger, A., Goodenough, J. B., Gendron, F. & Julien, C. M. Electronic, optical, and magnetic properties of $LiFePO_4$: small magnetic polaron effects. *Chem. Mater.* **19**, 3740–3747 (2007).
37. Xu, B. & Meng, S. Factors affecting Li mobility in spinel $LiMn_2O_4$—a first-principles study by GGA and GGA+U methods. *J. Power Sources* **195**, 4971–4976 (2010).
38. Soper, H. E., Young, A. W., Cave, B. M., Lee, A. & Pearson, K. On the distribution of the correlation coefficient in small samples. Appendix II to the Papers of "Student" and R. A. Fisher. *Biometrika* **11**, 328–413 (1917).
39. Rodgers, J. L. & Nicewander, W. A. Thirteen ways to look at the correlation coefficient. *Am. Stat* **42**, 59–66 (1988).
40. Xu, Z. & Zhu, H. Anion charge and lattice volume maps for searching lithium superionic conductors. *Chem. Mater.* **32**, 4618–4626 (2020).
41. Xu, Z., Chen, X., Chen, R., Li, X. & Zhu, H. Anion charge and lattice volume dependent lithium ion migration in compounds with fcc anion sublattices. *npj Comput. Mater.* **6**, 47 (2020).
42. Xu, Z.-M., Bo, S.-H. & Zhu, H. $LiCrS_2$ and $LiMnS_2$ cathodes with extraordinary mixed electron–ion conductivities and favorable interfacial compatibilities with sulfide electrolyte. *ACS Appl. Mater. Interfaces* **10**, 36941–36953 (2018).
43. Xu, Z., Chen, X., Zhu, H. & Li, X. Anharmonic cation-anion coupling dynamics assisted lithium-ion diffusion in sulfide solid electrolytes. *Adv. Mater.* **34**, e2207411 (2022).
44. Sun, Y. et al. Enhanced ionic conductivity and lack of paddle-wheel effect in pseudohalogen-substituted Li argyrodites. *Matter* **5**, 4379–4395 (2022).
45. Yamane, H. et al. Crystal structure of a superionic conductor, $Li_7P_3S_{11}$. *Solid State Ion.* **178**, 1163–1167 (2007).
46. Hart, G. L. W. & Forcade, R. W. Algorithm for generating derivative structures. *Phys. Rev. B* **77**, 224115 (2008).
47. Ong, S. P. et al. Python Materials Genomics (pymatgen): a robust, open-source python library for materials analysis. *Comput. Mater. Sci.* **68**, 314–319 (2013).
48. Kohn, W. & Sham, L. J. Self-consistent equations including exchange and correlation effects. *Phys. Rev.* **140**, A1133–A1138 (1965).
49. Blöchl, P. E. Projector augmented-wave method. *Phys. Rev. B* **50**, 17953–17979 (1994).
50. Perdew, J. P., Burke, K. & Ernzerhof, M. Generalized gradient approximation made simple. *Phys. Rev. Lett.* **77**, 3865–3868 (1996).
51. Hoover, W. G. Canonical dynamics: equilibrium phase-space distributions. *Phys. Rev. A* **31**, 1695 (1985).
52. Maintz, S., Deringer, V. L., Tchougreeff, A. L. & Dronskowski, R. LOBSTER: a tool to extract chemical bonding from plane-wave based DFT. *J. Comput. Chem.* **37**, 1030–1035 (2016).
53. Behler, J. & Parrinello, M. Generalized neural-network representation of high-dimensional potential-energy surfaces. *Phys. Rev. Lett.* **98**, 146401 (2007).
54. Dragoni, D., Daff, T. D., Csányi, G. & Marzari, N. Achieving DFT accuracy with a machine-learning interatomic potential: thermomechanics and defects in bcc ferromagnetic iron. *Phys. Rev. Mater.* **2**, 013808 (2018).
55. Shapeev, A. V. Moment tensor potentials: a class of systematically improvable interatomic potentials. *Multiscale Model. Simul.* **14**, 1153–1173 (2016).
56. Song, X. & Deng, C. Atomic energy in grain boundaries studied by machine learning. *Phys. Rev. Mater.* **6**, 043601 (2022).
57. Deng, Z., Chen, C., Li, X.-G. & Ong, S. P. An electrostatic spectral neighbor analysis potential for lithium nitride. *npj Comput. Mater.* **5**, 75 (2019).
58. Gubaev, K., Podryabinkin, E. V., Hart, G. L. W. & Shapeev, A. V. Accelerating high-throughput searches for new alloys with active learning of interatomic potentials. *Comput. Mater. Sci.* **156**, 148–156 (2019).
59. Novikov, I. S., Gubaev, K., Podryabinkin, E. V. & Shapeev, A. V. The MLIP package: moment tensor potentials with MPI and active learning. *Mach. Learn. Sci. Technol.* **2**, 025002 (2021).
60. Plimpton, S. Fast parallel algorithms for short-range molecular dynamics. *J. Comput. Phys.* **117**, 1–19 (1995).
61. Xu, Z. et al. Influence of anion charge on Li ion diffusion in a new solid-state electrolyte, Li_3LaI_6. *Chem. Mater.* **31**, 7425–7433 (2019).
62. Habasaki, J., León, C. & Ngai, K. L. *Dynamics of Glassy, Crystalline and Liquid Ionic Conductors: Experiments, Theories, Simulations* (Springer, 2017).
63. Landsberg, P. T. Einstein and statistical thermodynamics. III. The diffusion-mobility relation in semiconductors. *Eur. J. Phys.* **2**, 213–219 (1981).
64. Kuhn, A., Duppel, V. & Lotsch, B. V. Tetragonal $Li_{10}GeP_2S_{12}$ and Li_7GePS_8 – exploring the Li ion dynamics in LGPS Li electrolytes. *Energy Environ. Sci.* **6**, 3548 (2013).
65. Liu, Z. et al. Anomalous high ionic conductivity of nanoporous beta-Li_3PS_4. *J. Am. Chem. Soc.* **135**, 975–978 (2013).
66. Schlem, R., Banik, A., Ohno, S., Suard, E. & Zeier, W. G. Insights into the lithium sub-structure of superionic conductors Li_3YCl_6 and Li_3YBr_6. *Chem. Mater.* **33**, 327–337 (2021).

ACKNOWLEDGEMENTS

This work is supported by the Young Scientists Fund of the National Natural Science Foundation of China (22209074), the Fundamental Research Funds for the Central Universities (NO.NS2022059, NO.NS2021039), the Talent Research Startup Funds of Nanjing University of Aeronautics and Astronautics, the Jiangsu Funding Program for Excellent Postdoctoral Talent, and the Selected Funding for Scientific and Technological Innovation Projects for Overseas Students in Nanjing. This work is partially supported by High Performance Computing Platform of Nanjing University of Aeronautics and Astronautics.

AUTHOR CONTRIBUTIONS

Z.X., H.D., Z.D., and Y.L. performed all the calculations with the help of M.Z. and H.Z. Yinghui Xia contributed to the scientific discussion. Yongyao Xia conceived and designed the project. The manuscript was written by Z.X. and M.Z. with contributions from all authors.

COMPETING INTERESTS

The authors declare no competing interests.

ADDITIONAL INFORMATION

Supplementary information The online version contains supplementary material available at https://doi.org/10.1038/s41524-023-01049-w.

Correspondence and requests for materials should be addressed to Mingbo Zheng, Haitao Zhao or Yongyao Xia.

Reprints and permission information is available at http://www.nature.com/reprints

Publisher's note Springer Nature remains neutral with regard to jurisdictional claims in published maps and institutional affiliations.